Atomic-resolution incoherent high-angle annular dark field STEM images of Si(011)

K. Watanabe,[1] T. Yamazaki,[2] Y. Kikuchi,[3] Y. Kotaka,[3] M. Kawasaki,[4] I. Hashimoto,[2] and M. Shiojiri[5,6]

[1]*Tokyo Metropolitan College of Technology, 1-10-40 Higashiohi, Tokyo 140-0011, Japan*

[2]*Department of Physics, Science University of Tokyo, 1-3 Kagurazaka, Tokyo 162-8601, Japan*

[3]*Materials & Materials Engineering Laboratories, Fujitsu Laboratories Ltd., 10-1, Morinosato-Wakamiya, Atsugi 243-0197, Japan*

[4]*JEOL U.S.A., Inc. Massachusetts 01960*

[5]*Department of Anatomy, Kanazawa Medical University, Ishikawa 920-0293, Japan*

[6]*Kyoto Institute of Technology, Kyoto 606-8585, Japan*

Characteristic atomic-resolution incoherent high-angle annular dark field (HAADF) scanning transmission electron microscope (STEM) images of [011]-oriented Si have been experimentally obtained by a through-focal series. Artificial bright spots appear at positions where no atomic columns exist along the electron beam, in some experimental images. Image simulation, based on the Bloch wave description by the Bethe method, reproduces the through-focal experimental images. It is shown that atomic-resolution HAADF STEM images, which are greatly influenced by the Bloch wave field depending on the incident electron beam probe, cannot always be interpreted intuitively as the projected atomic images. It is also found that the atomic-resolution HAADF STEM images can be simply explained using the relations to the probe functions without the need for complex dynamical simulations.

PACS number(s): 61.66.−f, 68.37.Lp

I. INTRODUCTION

High-angle annular dark field (HAADF) scanning transmission electron microscope (STEM) images having better than 0.2-nm resolution have been demonstrated in a 100-keV electron microscope using a channeling wave packet along a low-order zone axis.[1,2] Subsequently, the HAADF STEM, with comparable resolution to high-resolution transmission electron microscopy (HRTEM), has been widely used to analyze crystal and defect structures in many materials.[3–8] The advantage of the HAADF STEM images is in giving a contrast depending on atomic number Z, because the intensity increases with Z^2 due to unscreened Rutherford scattering. Using this compositional dependence of the image contrast, we have obtained, at atomic resolution, the distribution of impurity Bi atoms around a grain boundary in a $SrTiO_3$ ceramic[9] and the distribution of As atoms doped in a Si wafer,[10] with the aid of image simulation. In these works, we showed that a simple estimation, assuming that the extra intensity is due entirely to the number and atomic number of impurity atoms, can be only used for a range of lower impurity concentrations and in a crystal without appreciable lattice distortion.

In order to describe the high-angle scattering of channeling electrons, the multiple scattering in the crystal must be taken into account. Since Kirkland, Loane, and Silcox simulated the visibility of single gold atoms on a Si(111) crystalline substrate,[11,12] many investigations have reported HAADF STEM image simulations. The basic methods used in these simulations can be classified into two types. One is the multislice method originated by Cowley and Moodie.[13] With the exception of Wang and Cowley's work,[14,15] in which both elastic and inelastic scattering were taken into account, most calculations have been carried out only using elastic scattering. This method can be readily applied to various objects with a supercell. It is, however, computationally inefficient, because the whole calculation has to be performed again and again for each probe position to yield an integrated beam diffraction intensity over an annular detector. The other is the Bloch wave method, in which images are calculated by dynamical elastic scattering[16] or using an ingenious assumption where each atom can be regarded as an independent incoherent scatterer.[17]

The simulations have demonstrated that the images are almost independent of sample thickness and probe-forming lens focus, so that the images can be intuitively interpreted without the need for simulations. In this way, extensive modelings of the image-formation process have been carried out but few experiments have asserted the importance of lens parameters (such as defocus, aperture size, and spherical aberration) and sample or illumination conditions (such as thickness and detector angle).[9,18] A clear understanding of the capabilities and limitations of HAADF STEM atomic-resolution images has not yet been established.

This paper shows characteristic atomically resolved HAADF STEM images of a [011]-oriented Si crystal experimentally obtained from a through-focal series. These images are accounted for by the simulation. In addition, the contrast of the images is related to the probe function. In Sec. II, the experimental procedure is presented. Section III derives the theory. The results and discussion are given in Sec. IV, and a conclusion is finally given in Sec. V.

II. EXPERIMENTAL PROCEDURE

Czochraski-grown [100]-oriented *p*-type silicon wafers with an electrical resistivity of 10 Ω cm were used in the present experiment. Specimens were prepared by mechanical polishing and two-step ion milling. The first ion milling was carefully carried out at angles as low as possible with 4-keV Ar ions, and the second step was 1.7-keV Ar ion milling so as to remove the amorphous and oxide surface layers.
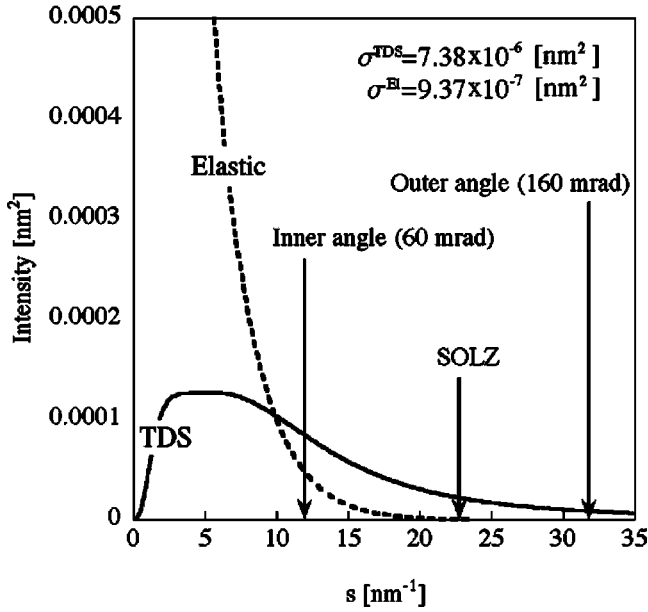
63 085316-1

FIG. 1. Intensities of elastic scattering (dotted line) and thermal diffuse scattering (solid line) from a Si atom. The three arrows show the positions of the inner angle of the annular detector, the outer one, and the SOLZ line.

HAADF STEM observations were performed with a JEM-2010F-TEM/STEM, operated at 200 keV. The spherical aberration C_s and the semiangle α of the probe-forming lens were 1.0 mm and 12 mrad, respectively. The angular range of the annular detector used was 60–160 mrad. Image processing was performed by Fourier filtering, where a mask of 2 nm^{-1} diam was used for each spot in a diffractogram of the image. Alterning mask size, from 2 to 3 nm^{-1}, does not have much of an effect on the final conclusion.

Using the electron beam that had passed through the detector aperture, parallel electron-energy-loss spectroscopy (PEELS) was simultaneously carried out to estimate the sample thickness. The PEELS was acquired with a Gatan Digi PEELS model 766 estimated and provides an estimate of sample thickness to be 90 nm at the observed area.

III. THEORY

For the calculation of the crystal potential and thermal diffuse scattering (TDS), the atomic scattering factor of Si by Weickenmeier and Kohl[19] and a Debye-Waller factor of 0.0045 nm^2 by Rossouw *et al.*[20] were used. Figure 1 shows the elastic scattering intensity and the TDS intensity for a Si atom, together with the cross sections of elastic scattering σ^{el} and TDS σ^{TDS}. The cross section of TDS is about eight times as large as that of elastic scattering. Therefore, even if second-order Laue zone (SOLZ) lines are placed on the present annular detector, the TDS provides the main contribution to the formation of HAADF STEM images.

The coherent convergent probe intensity or probe function $P(\mathbf{R}, \mathbf{R}_0)$ at $\mathbf{R}$ on the object surface is represented by a superposition of plane waves modulated by the lens aberration function $W(\mathbf{K}_\parallel)$:

$$P(\mathbf{R}, \mathbf{R}_0) = \left| \int_{\text{probe}} \exp\{i\mathbf{K}_\parallel \cdot (\mathbf{R} - \mathbf{R}_0)\} \exp\{iW(\mathbf{K}_\parallel)\} d\mathbf{K}_\parallel \right|^2,$$

(1)

where $\mathbf{R}_0$ is the center of the incident probe and $\mathbf{K}_\parallel$ is the transverse component of the partial incident plane wave. A wave packet $\Psi(\mathbf{R} - \mathbf{R}_0, z)$ at a depth of z in a crystal formed by the probe function is given by

$$\Psi(\mathbf{R} - \mathbf{R}_0, z) = \int_{\text{probe}} \sum_j \varepsilon^j(\mathbf{K}_\parallel) \tau^j(\mathbf{R}, \mathbf{K}_\parallel)$$
$$\times \exp\{i(k_z + \gamma^j)z\} \exp(-\mu^j z)$$
$$\times \exp\{i\mathbf{K}_\parallel \cdot (\mathbf{R} - \mathbf{R}_0)\} \exp\{iW(\mathbf{K}_\parallel)\} d\mathbf{K}_\parallel,$$

(2)

where τ^j is a two-dimensional (2D) Bloch state, $k_z + \gamma^j$ is the transverse wave number, ε^j is the excitation amplitude, and μ^j is the absorption coefficient for each branch j. According to the simulation proposed by Pennycook and Jesson,[17] the intensity $I(\mathbf{R}_0, t)$ in the incoherent HAADF STEM image, caused by TDS, can be written by using the δ-function approximation:

$$I(\mathbf{R}_0, t) = \sum_{(i,k)} \int_0^t \sigma_{(i,k)} |\Psi(\mathbf{R}_i - \mathbf{R}_0, z)|^2 \delta(z - z_{(i,k)}) dz,$$

(3)

where t is the sample thickness, $\mathbf{R}_i$ is the position vector of the i column, and $\sigma_{(i,k)}$ is the TDS cross section for the kth atom on the i column. Equation (3) is based on an assumption that the electrons are kinematically scattered due to TDS toward high angles. This is a reasonable approximation for not so thick samples since the intensity of scattered electrons is a small fraction of that of the total wave function in a crystal because of the small TDS absorption. The cross section was calculated by the Einstein model.[21]

IV. RESULTS AND DISCUSSION

Figure 2 shows experimental through-focal HAADF STEM images, together with their processed versions and the corresponding simulated images. The image processing provided valuable images by decreasing the noise drastically, and thereby enhancing detailed structure. As the defocus value increases from $\Delta f = -40$ nm to $\Delta f = -65$ or -75 nm, unresolved bright spots in a dumbbell change into clearly resolved ones and a significant artificial or false spot appears at the center of the sixfold structure. The images in Figs. 2(d) and 2(g) are slightly deformed and show a small deviation from the regular bright spot positions, which may be due to a small drift or vibration of the detector and/or specimen during the observation. In any case, the simulation, where the defocus steps coincide with the steps for the experimental through-focal images, reproduces these three experimental images quite well. In the simulation, a sample thickness of 90 nm, which was evaluated from PEELS, was used. Similar atomic resolved through-focal images were observed at areas with different thickness in the same sample. Detailed discus-
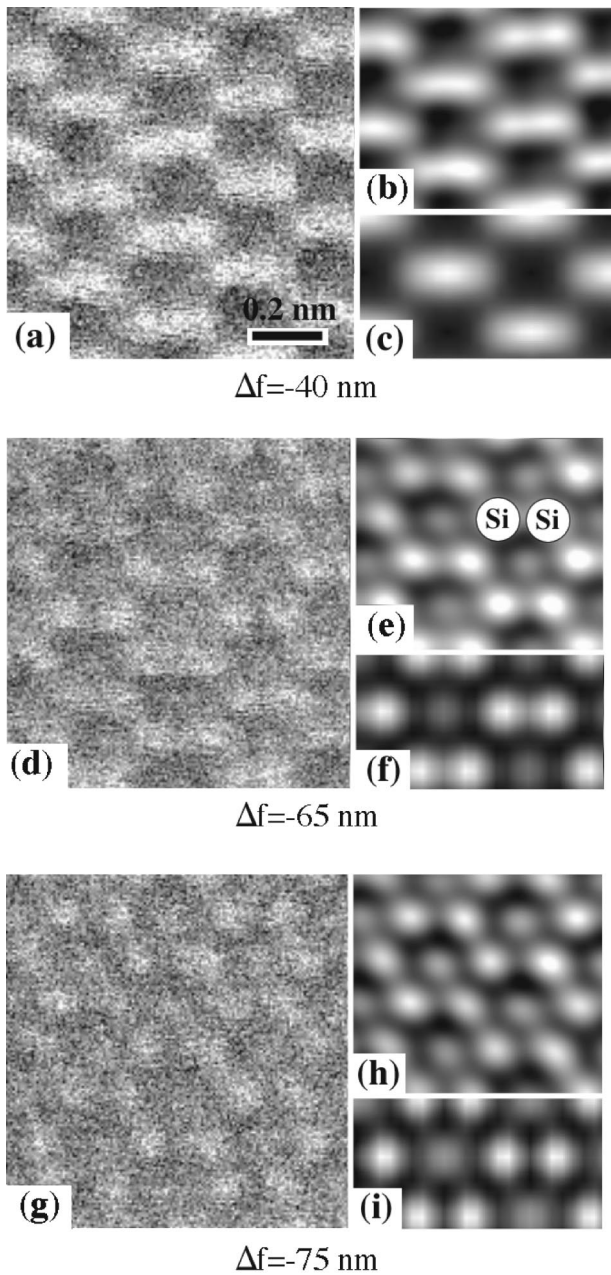
FIG. 2. The observed HAADF STEM images [(a), (d), and (f)], their processed images [(b), (e), and (h)], and the corresponding simulated images [(c), (f), and (i)]. The calculations were made by $\Delta f = -40$ nm (c), -65 nm (f), and -75 nm (i), respectively.
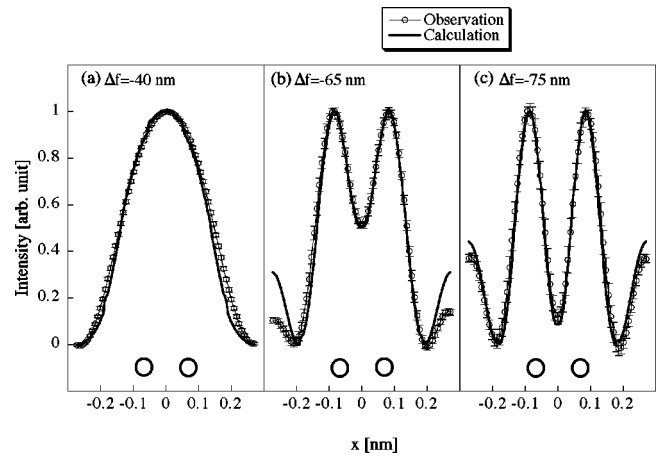

FIG. 3. Observed intensity profiles deduced by processing and averaging 16 spots with error bars and simulated intensity profiles in Figs. 2(c), 2(f), and 2(i). The open circles denote the positions of the atomic columns.

sion on the thickness effect on the image contrast is reported elsewhere.

Figure 3 illustrates an averaged line profile from 16 bright spots in each processed image in Fig. 2. These experimental line profiles are also in good agreement with the corresponding simulated line profiles, although there is little deviation in the intensity at the artificial bright spot positions of $x = \pm 0.28$ nm in Fig. 3.

The contrast of the HAADF STEM image of a simple substance such as Si, having a constant cross section, depends only on the intensity of the wave field at each atom position on columns, as seen from Eq. (3). In order to discuss the formation of dumbbell images shown in Figs. 2(a) and 2(d), we have calculated the intensities of the wave fields, using Eq. (2), at different depths using different probe functions at various foci. The calculations were made for cases where the probes are located at the position of the atomic column (i) [see Fig. 4(a)] and the center of the dumbbell (ii) [see Fig. 4(b)]. At $\Delta f = -40$ nm, the probe (i) forms a strong wave field at the probe-located column and a weak field at its nearest column, and then the field intensity changes from the former to the latter with increasing depth, as seen in Fig. 4(e).[22] Figure 4(f) reveals that probe (ii) forms a strong wave field at the two nearest-neighbor columns. As a whole, however, there is no clear difference in resultant intensity between the wave fields on columns produced by these two probes (i) and (ii). Hence, the TDS scattering caused by the wave field is almost the same in intensity between these two cases and, consequently, the unresolved dumbbell images appear as seen in Figs. 2(a)–2(c). On the other hand, the intensities of the wave fields caused by probes (i) and (ii) are greater and weaker at a low value of underfocus ($\Delta f = -65$ nm) than those at $\Delta f = -40$ nm, respectively, as seen in Figs. 4(e)–4(h). As a result, atomic-resolved dumbbell images appear as shown in Figs. 2(d)–2(i).

These image characteristics can be simply related to the incident probe function.[23,24] The probe at $\Delta f = -40$ nm is close to Gaussian in nature. Its full width at half maximum is so large that when it is located on the center of a dumbbell, it covers the two atom columns under its tail and causes a rather strong wave field through the columns [see Fig. 4(d)]. On the contrary, the probe at a lower underfocus value develops a sharper peak 1.4 times as strong as that of the probe at $\Delta f = -40$ nm, so that when it is located on an atomic column it makes a much stronger field through this column [see Fig. 4(c)]. However, when it is located on the center of a dumbbell, its tail produces a weak field at the two columns.

The same simulation on the center of the sixfold structure is displayed in Fig. 5 in order to interpret the appearance of the artificial bright spots. The probe at a low underfocus of $\Delta f = -75$ nm (and also $\Delta f = -65$ nm) has not only a sharper
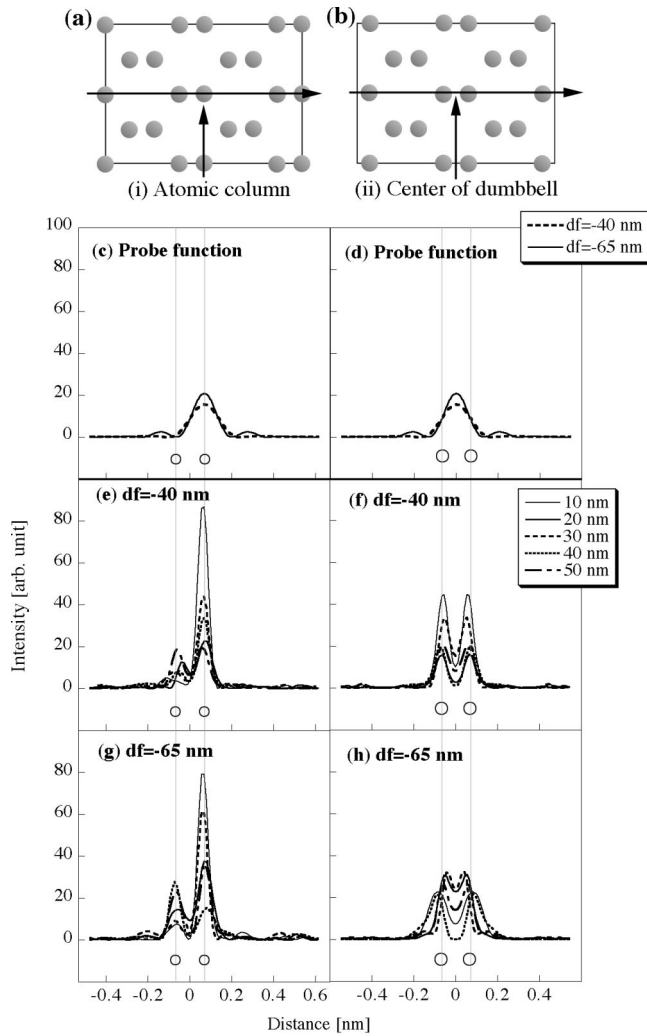
FIG. 4. Projections of a Si crystal along the [011] direction together with probe positions (a) and (b). The intensities of the probe function located on an atomic column and the center of a dumbbell (c) and (d). Intensity of the wave fields of various thickness, at $\Delta f = -40$ nm [(e),(f)] and -65 nm [(g),(h)]. In (c)–(h), positions of atomic columns for a dumbbell are denoted by open circles.

main peak but also an appreciable subsidiary peak around the main peak, as seen in Fig. 5(b).

When this probe is located on the center of the sixfold structure (iii) [see Fig. 5(a)], the subsidiary peak is positioned at the six nearest-neighbor atomic columns. The wave field formed by the probe is trapped at these columns [see Fig. 5(d)], and the high-angle TDS from atoms on the columns was accordingly counted ''as a signal from the center'' by the annular detector. This is the reason why the artificial bright spot appears at the center of the sixfold structure as shown in Figs. 2(d)–2(i). It is clear from Figs. 5(b) and 5(c) that the probe at $\Delta f = -40$ nm, which has a very small subsidiary peak, does not produce the artificial spots. The appearance of these artificial spots indicates strongly that atomic resolved HAADF images cannot always be interpreted intuitively as the projected atomic images or structural and compositional images.
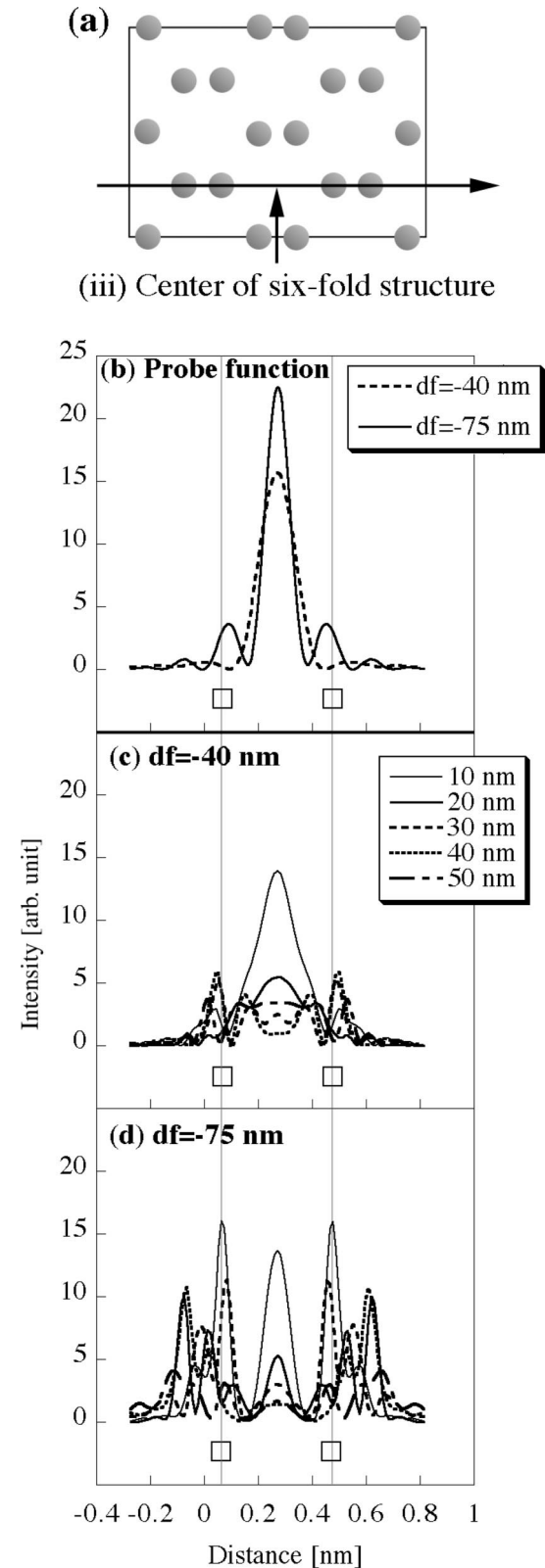

FIG. 5. Projection of a Si crystal along the [011] direction and probe position (a). The intensity of the probe function located on a sixfold structure (b). Intensities of the wave fields of various thickness, at $\Delta f = -40$ nm (c) and -75 nm (d). In (b)–(d), the positions of nearest-neighbor atomic columns around the probe are denoted by open squares.

The optimum probe for the intuitive image interpretation is one with a sharp central peak but no significant subsidiary peaks at nearest-neighbor columns.[23]

V. CONCLUSIONS

Characteristic atomic resolved HAADF STEM images of Si (011), some of which exhibit artificial bright spots, are presented from an experimental through-focal series. The experimental images are confirmed to be incoherent HAADF STEM images, because TDS is the main contribution to the image formation under a selected higher annular detector range of 60–160 mrad. From a detailed comparison between experimental images and simulated ones based on the Bloch wave description, it is found that images with artificial bright spots appear under some observation conditions in addition to the intuitively interpreted images. It is also shown that the characteristics of these HAADF STEM images can be simply explained using the relation to the probe function without need of simulations.

[1] D. H. Shin, E. J. Kirkland, and J. Silicox, Appl. Phys. Lett. **55**, 2456 (1989).

[2] P. Xu, E. J. Kirkland, J. Silicox, and R. Kyse, Ultramicroscopy **32**, 93 (1990).

[3] M. F. Chisholm, A. Maiti, S. J. Pennycook, and S. T. Pantelides, Phys. Rev. Lett. **81**, 132 (1998).

[4] M. M. Mcgibbon, N. D. Browing, M. F. Chisholm, A. J. Mcgibbon, S. J. Pennycook, V. Ravikuma, and V. P. Dravid, Science **266**, 102 (1994).

[5] A. J. Mcgibbon, S. J. Pennycook, and J. E. Angelo, Science **269**, 519 (1995).

[6] K. Mitsuishi, M. Kawasaki, M. Takeguchi, and K. Furuya, Phys. Rev. Lett. **82**, 3082 (1999).

[7] A. Maiti, S. T. Pantelides, M. F. Chisholm, and S. J. Pennycook, Appl. Phys. Lett. **75**, 2380 (1999).

[8] Y. Yan, M. M. Al-Jessim, Z. Xu, X. Lu, D. Viehalnd, M. Payne, and S. J. Pennycook, Appl. Phys. Lett. **75**, 1961 (1999).

[9] M. Kawasaki, T. Yamazaki, S. Sato, K. Watanabe, and M. Shiojiri, Philos. Mag. A **81**, 245 (2001).

[10] T. Yamazaki, K. Watanabe, Y. Kikuchi, M. Kawasaki, I. Hashimoto, and M. Shiojiri, Phys. Rev. B **61**, 13833 (2000).

[11] E. J. Kirkland, R. F. Loane, and J. Silcox, Ultramicroscopy **23**, 77 (1987).

[12] R. F. Loane, E. J. Kirkland, and J. Silcox, Acta Crystallogr., Sect. A: Found. Crystallogr. **44**, 912 (1988).

[13] J. M. Cowley and A. F. Moodie, Acta Crystallogr. **10**, 609 (1957).

[14] Z. L. Wang and J. M. Cowley, Ultramicroscopy **31**, 437 (1989).

[15] Z. L. Wang and J. M. Cowley, Ultramicroscopy **32**, 275 (1990).

[16] P. D. Nellist and S. J. Pennycook, Ultramicroscopy **78**, 111 (1999).

[17] S. J. Pennycook and D. E. Jesson, Phys. Rev. Lett. **64**, 938 (1990).

[18] T. Yamazaki, K. Watanabe, A. Recnik, M. Ceh, M. Kawasaki, and M. Shiojiri, J. Electron Microsc. **49**, 753 (2000).

[19] A. Weickenmeier and H. Kohl, Acta Crystallogr., Sect. A: Found. Crystallogr. **47**, 590 (1991).

[20] C. J. Rossouw, P. Spellward, D. D. Perovis, and D. Cherns, Philos. Mag. A **69**, 255 (1994).

[21] S. J. Pennycook and D. E. Jesson, Ultramicroscopy **37**, 14 (1991).

[22] J. Fertig and H. Rose, Optik (Stuttgart) **59**, 407 (1981).

[23] S. J. Pennycook and P. D. Nellist, *Impact of Electron and Scanning Probe Microscopy on Materials Research* (Kluwer, Dordrecht, 1999), pp. 161–207.

[24] J. Liu and J. M. Cowley, Ultramicroscopy **52**, 335 (1993).